JACS
JOURNAL OF THE AMERICAN CHEMICAL SOCIETY
Article
pubs.acs.org/JACS

Strong Covalency-Induced Recombination Centers in Perovskite Solar Cell Material $CH_3NH_3PbI_3$

Michael L. Agiorgousis,[†] Yi-Yang Sun,*[,†] Hao Zeng,[§] and Shengbai Zhang*[,†]

[†]Department of Physics, Applied Physics & Astronomy, Rensselaer Polytechnic Institute, Troy, New York 12180, United States
[§]Department of Physics, University at Buffalo SUNY, Buffalo, New York 14260, United States

Supporting Information

ABSTRACT: Inorganic−organic hybrid perovskites are a new family of solar cell materials, which have recently been used to make solar cells with efficiency approaching 20%. Here, we report the unique defect chemistry of the prototype material, $CH_3NH_3PbI_3$, based on first-principles calculation. We found that both the Pb cations and I anions in this material exhibit strong covalency as characterized by the formation of Pb dimers and I trimers with strong covalent bonds at some of the intrinsic defects. The Pb dimers and I trimers are only stabilized in a particular charge state with significantly lowered energy, which leads to deep charge-state transition levels within the band gap, in contradiction to a recent proposal that this system has only shallow intrinsic defects. Our results show that, in order to prevent the deep-level defects from being effective recombination centers, the equilibrium carrier concentrations should be controlled so that the Fermi energy is about 0.3 eV away from the band edges. Beyond this range, according to a Shockley−Read−Hall analysis, the non-equilibrium carrier lifetime will be strongly affected by the concentration of I vacancies and the anti-site defects with I occupying a CH_3NH_3 site.

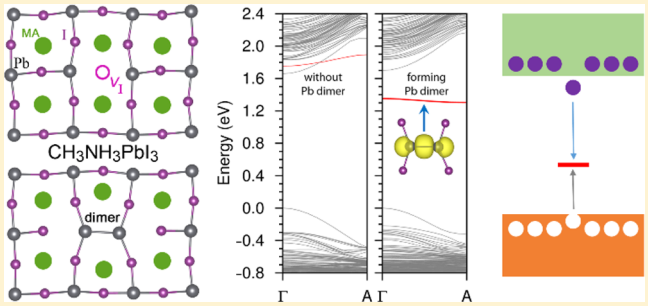

INTRODUCTION

Photovoltaic (PV) generation of electricity by harvesting solar energy offers a promising solution for renewable energy. The high cost of current PV technology, however, is a major obstacle for large-scale deployment of solar power plants. The search for inexpensive solar cell materials made of earth-abundant elements has been a topic of extensive study across the globe. In addition, low-cost synthesis of such materials, e.g., solution-based methods, is also the key for lowering the overall cost of the PV technology. Materials prepared by such low-cost methods are usually defective. It seems ambitious to expect that solar cells made from such defective materials generate power conversion efficiency (PCE) comparable to those of solar cells based on highly crystalline solar materials, e.g., silicon. Research in the past year, however, has demonstrated high PCE achieved by combining earth-abundant elements and low-cost processing methods.

The breakthrough was based on the organic−inorganic hybrid perovskite solar materials, as represented by $CH_3NH_3PbI_3$, which only consist of earth-abundant elements. When used as absorbers in solar cells, they have reached 15% PCE.[1,2] Several reports with higher PCEs (approaching 20%) have appeared very recently.[3,4] Importantly, the high PCEs have been achieved using both dye-sensitized[1,4] and planar[2,3] solar cell structures and various low-cost synthesis techniques.[5−7] Considering that these materials were proposed for solar cell application only 5 years ago with an initial PCE of 3.8%,[8] the fast growth of this field suggests a great potential for future deployment of this technology at the industrial level.

Structural defects ranging from point defects to grain boundaries are often among the most important factors affecting the performance of solar cell materials grown by low-cost techniques. The success of II−VI semiconductors, such as $Cu(In,Ga)Se_2$ and CdTe, in thin-film solar cells is usually attributed to the benign defects (or defect tolerance) of such materials.[9,10] In contrast, Si and III−V semiconductors lack this property. Therefore, high purity and high crystallinity of these materials are required in solar cells to achieve high efficiency. The high efficiency in perovskite solar cell materials has been attributed to various characteristics, including long carrier diffusion lengths,[11,12] low recombination rates,[13,14] sharp optical absorption edge,[15] and the existence of ferroelectric domains.[16] Because both the carrier diffusion lengths and the recombination rates are intimately related to defects in the materials, a full understanding of the defect physics and chemistry in these materials is not only of great fundamental interest but also highly desirable in the design of strategies for further improving the PCE and replacing Pb with environmentally friendly elements.[17,18]

So far, defects in the perovskite solar cell materials have only received limited study,[19,20] suggesting an absence of deep-level defects. In this article, using first-principles calculations, we

Received: August 2, 2014
Published: September 22, 2014

   dx.doi.org/10.1021/ja5079305 | J. Am. Chem. Soc. 2014, 136, 14570−14575

show that the prototype perovskite solar cell material, $CH_3NH_3PbI_3$, exhibits rich and unique defect chemistry that does not exist in traditional solar cell materials. Previous studies have suggested that $CH_3NH_3PbI_3$ is an ionic material showing very weak covalence.[19] In contrast, we have identified strong covalency of both the Pb cations and I anions in $CH_3NH_3PbI_3$, which is characterized by the formation of Pb dimers and I trimers. A critical consequence of the strong covalency on the solar cell performance is that some intrinsic point defects could be significantly stabilized at certain charge states, giving rise to deep charge-state transition levels within the band gap that could serve as recombination centers (RCs) for photogenerated carriers. In order to prevent such deep-level defects from being effective RCs, our study suggests that the materials should be grown in a lightly doped region with the Fermi level not too close to the band edges.

COMPUTATIONAL METHODS

Our first-principles calculation was based on the density functional theory (DFT) as implemented in the VASP program.[21] The generalized gradient approximation of Perdew, Burke, and Ernzerhof (PBE)[22] was used for the exchange-correlation functional. We take advantage of the PBE calculation, yielding a band gap of about 1.63 eV for $CH_3NH_3PbI_3$ in good agreement with experimental value of 1.57 eV.[23] Based on recent studies using quasi-particle GW method,[24,25] this agreement on the calculated band gap is a result of error cancellation, i.e., an underestimation due to the standard DFT band gap error and an overestimation due to the exclusion of spin−orbit coupling (SOC). We have checked that by including the SOC, the change in calculated atomic forces is negligibly small, which justifies the optimized structures by excluding the SOC.

A 2×2×2 supercell, as shown in Figure 1, was used to study the bulk properties of $CH_3NH_3PbI_3$. We adopted the tetragonal structure and

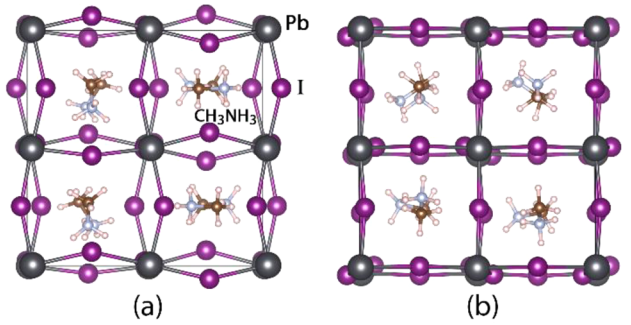

Figure 1. Atomic structure of $CH_3NH_3PbI_3$ viewed along the *c*-axis (a) and the direction perpendicular to the *c*-axis (b).

the lattice constants (a = 12.52 Å and c = 12.66 Å) from experiment without further optimization.[26] Strictly, with respect to the tetragonal unit cell, the supercell shown in Figure 1 is $c(2\times2)$ in the *a*-*b* plane and 1× along the *c*-axis. For convenience, however, we label the supercells in this work (i.e., 2×2×2 mentioned above or 4×4×4 below for defect calculations) with respect to the smaller cubic cell containing only one formula of $CH_3NH_3PbI_3$.

The internal coordinates were optimized using the simulated annealing (SA) method as implemented in the VASP code. The SA simulations were started from four different initial structures. Each simulation underwent 50 000 molecular dynamics (MD) steps with temperature cooled down from 350 to 0 K. Three of the simulations reached low-energy structures with the total energy difference smaller than 3 meV per 2×2×2 supercell. One of the structures is shown in Figure 1. The main difference between the three low-energy structures is the orientation of the CH_3NH_3 ions (methylammonium, or MA in short). It was found that the defect properties reported later were insensitive to the MA orientations.

In the defect calculations, we started from the 2×2×2 supercell combined with a single special *k*-point at ($^1/_2$, $^1/_2$, $^1/_2$) representing the Brillouin zone. This setup allows us to perform SA calculations, which were found to be important in searching the configuration space and possible non-intuitive defect structures, as described below. Each SA run contains 35 000 MD steps with temperature cooled down from 350 to 0 K. Once the low-energy defect configuration was found, more accurate calculations to obtain the defect formation energy and defect transition level were carried out using a much larger 4×4×4 supercell containing 768 atoms (i.e., 64 $MAPbI_3$ formulas) and the Γ point representing the Brillouin zone. Projector augmented wave (PAW) potentials[27] were used to describe the core−valence interaction. Plane-waves with kinetic energy up to 408 eV were used as the basis set. The atomic structures were relaxed until the residual forces on all atoms were smaller than 0.025 eV/Å.

RESULTS AND DISCUSSION

Deep Defect Transition Levels. The focus of our study on defects in $MAPbI_3$ was to identify possible intrinsic RCs in this material. According to the Shockley−Read−Hall (SRH) theory of recombination,[28] effective RCs can only be neutral and singly charged defects. For higher charged defects, the recombination process involves the capture of charge carriers by repulsive centers (i.e., electron capture by a negatively charged defect or hole capture by a positively charged defect), which has a cross section at least 5−7 orders of magnitude smaller than that for a neutral or attractive center.[29] For this reason, we calculated the defect transition levels, $\varepsilon(0/-)$ and $\varepsilon(0/+)$, for 12 intrinsic defects according to $\varepsilon(0/-) = E_D^- - E_D^0 - E_{VBM}$ and $\varepsilon(0/+) = E_D^0 - E_D^+ - E_{VBM}$,[30−32] where E_D^q is the total energy of the supercell containing a defect in the charge q state and E_{VBM} is the energy of valence band maximum (VBM), as calculated using a supercell that does not contain any defect. The defect transition levels thus calculated are responsible for the recombination rate in an SRH process.[33]

Figure 2 shows the calculated $\varepsilon(0/-)$ and $\varepsilon(0/+)$ levels in blue and brown, respectively. In typical compound semi-

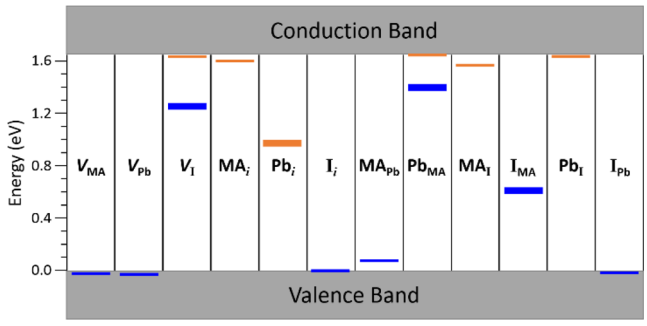

Figure 2. Calculated charge-state transition levels within the band gap for 12 intrinsic defects in $CH_3NH_3PbI_3$. The $\varepsilon(0/-)$ and $\varepsilon(0/+)$ levels are shown in blue and brown, respectively. Deep levels are marked by thicker bars.

conductors, cation vacancies and anion interstitials are acceptors, while cation interstitials and anion vacancies are donors. An anti-site defect can be qualitatively viewed as a pair of vacancy and interstitial defects to judge if it is a donor or an acceptor. However, two defects in Figure 2, namely I vacancy (V_I) and Pb-on-MA anti-site (Pb_{MA}), which are normally donors, exhibit deep $\varepsilon(0/-)$ transition levels, i.e., deep acceptor levels. Other than these two deep-level defects, Pb interstitial

dx.doi.org/10.1021/ja5079305 | J. Am. Chem. Soc. 2014, 136, 14570−14575

(Pb_i) and I-on-MA anti-site (I_{MA}) also show deep $\varepsilon(0/+)$ and $\varepsilon(0/-)$ transition levels, respectively. Whether these defect levels could become effective as RCs depends on two factors: (1) they are stable in neutral or a singly charged state, and (2) they have a relatively low formation energy to exist in a significant amount. Before addressing these issues by a detailed analysis, we first study the origin of these deep levels.

Strong Covalency. We first discuss the case of V_I. For a typical shallow donor, only the $\varepsilon(0/+)$ transition level matters, while its $\varepsilon(0/-)$ level should be located at the conduction band minimum (CBM) because the charge transition involves the capture of an extra electron and there is no level in the band gap to accept this electron. For V_I, however, we found that once the defect becomes negatively charged, the structure undergoes a significant distortion, as shown in Figure 3a. After capturing an extra electron (i.e., with two electrons at the CBM), the two Pb atoms that are originally separated by the vacancy move toward each other and form a dimer. It is noted that if the relaxation starts from the structure shown in the left panel of Figure 3a, the Pb dimer does not form. The dimer formation was observed in the SA calculation when ramping up the system temperature to 350 K and then cooled down to 0 K, as described in the Computational Methods section.

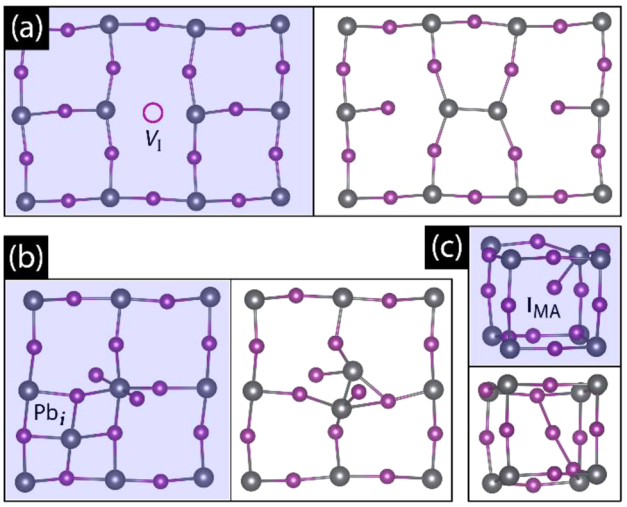

Figure 3. Atomic structure change before (shaded) and after (non-shaded) the formation of a Pb dimer for V_I (a), Pb_i (b), and an I trimer (c).

As can be seen from the band structure plot in Figure 4a, the formation of the Pb dimer creates a deep defect level in the band gap. Thus, the two electrons occupying the CBM before the formation of Pb dimer drop to this gap level, which significantly lowers the energy in the −1 charge state and move the $\varepsilon(0/-)$ transition level from the CBM to 0.38 eV below the CBM (or 1.25 eV above the VBM).

The formation of a Pb dimer was also observed for Pb_i and Pb_{MA} defects. Pb_i is a double donor and in the neutral state already has two electrons occupying the CBM like the case of V_I in −1 charge state. The atomic structures before and after the formation of Pb dimer are shown in Figure 3b. Similar to V_I, the formation of a Pb dimer creates a gap level occupied by two electrons, which lowers the energy of the neutral charge state and cause a deep donor level in the band gap. For Pb_{MA}, our calculation shows that it is actually a defect complex of Pb_i and MA vacancy (V_{MA}). Since V_{MA} is a shallow acceptor (see Figure 2), which takes one electron from Pb_i, the behavior of Pb_{MA} is similar to V_I, which will be discussed again later.

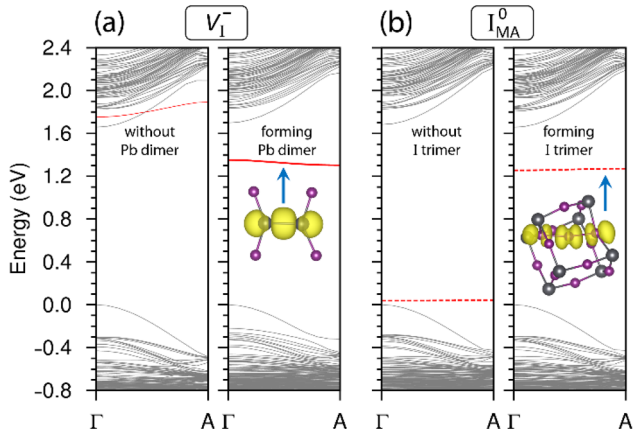

Figure 4. Band structure plot for V_I^- (a) and I_{MA}^0 (b) from Γ to ($^1/_2$, $^1/_2$, $^1/_2$). For V_I^- without forming a Pb dimer, there is a defect band in strong resonance with the host bands, which is shown by a thin red line. After forming a Pb dimer, the doubly occupied band in the band gap is shown by a thick red line. For I_{MA}^0, before forming an I trimer, there is an empty defect band close to the bulk VBM, shown by a dashed red line. After the formation of an I trimer, the defect band is lifted up to near the CBM. The insets show the charge density contour plot for the defect bands after forming a Pb dimer and an I trimer.

The cause of the deep level of I_{MA} is different from the above cases. Instead, it was found that the deep level resulted from the formation of an I trimer in the neutral state, as shown in Figure 3c, where the I atom occupying a MA site is located between two I atoms on the lattice. As can be seen in Figure 4b, opposite from the case of V_I, the formation of an I trimer significantly lifts up an empty level, which was originally located right above the VBM, to a high energy position in the band gap, suggesting the formation of a new chemical bond that lowers the energy of I_{MA} in the neutral state and gives rise to the deep $\varepsilon(0/-)$ transition level.

Both the formation of a Pb dimer and an I trimer indicates strong covalency in $MAPbI_3$, which as a halide is usually considered to be an ionic material exhibiting weak covalency. The insets in Figures 4a,b show the charge density plots for the band gap states of V_I and I_{MA} after the formation of a Pb dimer and an I trimer, respectively. It can be seen that the state for V_I is clearly a bonding $p-p$ σ bond, while the state for I_{MA} is an antibonding σ bond involving the p orbitals of all the three I atoms. Such strong covalent bonding between cations and anions could be observed on the surfaces of group-IV and III–V semiconductors,[34] but has rarely been known for intrinsic defects in semiconductors.

The formation of the covalent bond is in a competition with the strain caused by structural distortion, as can be seen in Figure 3. The strength of the covalent bonding depends on the charge state of the defects. For example, the Pb dimer can only be stabilized in the −1 charge state of V_I and the neutral state of Pb_i. In the corresponding ionized charged state, i.e., neutral for V_I and +1 for Pb_i, the bonding orbital is occupied by only one electron so that the energy gain is much smaller and the structures with and without the Pb dimer become nearly equally stable. This result is further evidence of the covalency in the dimer or trimer bonding.

Defect Formation Energy. As mentioned earlier, in order to examine whether the deep-level defects discussed above

dx.doi.org/10.1021/ja5079305 | J. Am. Chem. Soc. 2014, 136, 14570–14575

could become effective RCs, we need to know the thermodynamic stability of these defects and the relative stability of a defect among different charge states. For this purpose, we calculate the defect formation energy for these defects. Following the established method,[30−32,35] the formation energy (ΔH) of a defect in the q charge state is defined as

$$\Delta H = E_D{}^q - E_0 + \sum_i n_i\mu_i + q(E_{VBM} + E_F)$$

where $E_D{}^q$ is the same as defined earlier for calculating transition levels, E_0 is the total energy of a defect-free supercell, E_F is the Fermi energy measured from E_{VBM}, μ_i is the atomic chemical potential, and n_i is the number of atoms i being exchanged during the defect formation between the host and the atomic reservoir of energy μ_i per atom. According to this definition, ΔH is a function of μ_i and E_F, where E_F is usually treated as a variable between 0 eV and the band gap E_g. We next determine the allowed region for μ_i in the three-dimensional space spanned by the chemical potentials μ_{MA}, μ_{Pb}, and μ_I, as shown in Figure 5a. Here, we treat MA as a whole with a molecular chemical potential of μ_{MA}.

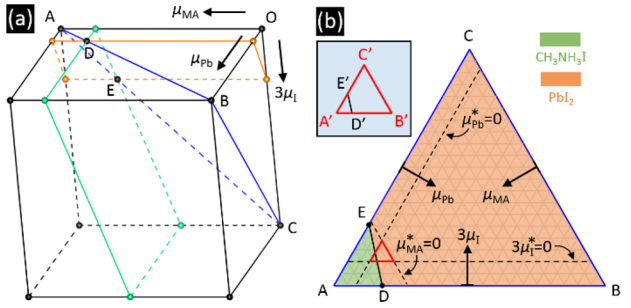

Figure 5. (a) Atomic potential space spanned by μ_{MA}, μ_{Pb}, and μ_I. The constraints set by the primary phase $CH_3NH_3PbI_3$ and the two secondary phases CH_3NH_3I and PbI_2 are represented by blue, green and brown planes, respectively. (b) Triangle diagram showing the allowed region for the three chemical potentials. The constraints set by three elementary secondary phases (i.e., bulk phases of MA, Pb, and I) are shown by dashed lines, which demarcate a smaller trianglar region. A zoom-in view of the small triangle region with labels of important points is shown in the inset. Taking the dashed lines as references of μ_i* (i.e., μ_i* = 0 on the corresponding lines), the chemical potentials (μ_{MA}*, μ_{Pb}*, and 3 μ_I*) at D′ and E′ are (−2.82 eV, −1.70 eV, 0 eV) and (−1.97 eV, 0 eV, −2.55 eV), respectively.

Under thermal equilibrium with $MAPbI_3$, it is required that $\mu_{MA} + \mu_{Pb} + 3\mu_I = E(MAPbI_3)$, where $E(MAPbI_3)$ is the total energy per formula of bulk $E(MAPbI_3)$. With this constraint, the allowed values for the μ_i must be located on the equilateral triangle ABC in Figure 5a. In order to avoid the formation of secondary phases, the conditions $\mu_{MA} + \mu_I \le E(CH_3NH_3I)$ and $\mu_{Pb} + 2\mu_I \le E(PbI_2)$ must also be satisfied, where $E(CH_3NH_3I)$ and $E(PbI_2)$ are the total energy per formula for the stable bulk phase of CH_3NH_3I[36] and PbI_2,[37] respectively. The highest allowed values satisfying these two conditions are marked by green and brown planes in Figure 5a, respectively. The allowed region for μ_i is thus considerably reduced, as shown in the triangle plot in Figure 5b, where the overlap between the CH_3NH_3I and PbI_2 phases is the region in which $MAPbI_3$ is thermodynamically more stable than the two secondary phases. Our calculation shows that the overlap region is very narrow and can be approximately represented by the line of DE, which is a result of the small enthalpy of formation of $MAPbI_3$ (calculated to be 0.025 eV per formula) from the two secondary phases. Further considering the elemental secondary phases, as represented by the dashed lines in Figure 5b, the allowed regions is further reduced to the line of D′E′ (see the inset). In constructing the plot, we consider bulk I_2,[38] metal Pb in *fcc* structure, and MA in an artificial monoclinic structure. From Figure 5b, one can see that the final allowed region for μ_i (i.e., the D′E′ line) is unlikely to be affected by the choice of MA phase.

The calculated defect formation energy for the four defects are shown in Figure 6 as a function of E_F. For V_I, Pb_i and Pb_{MA},

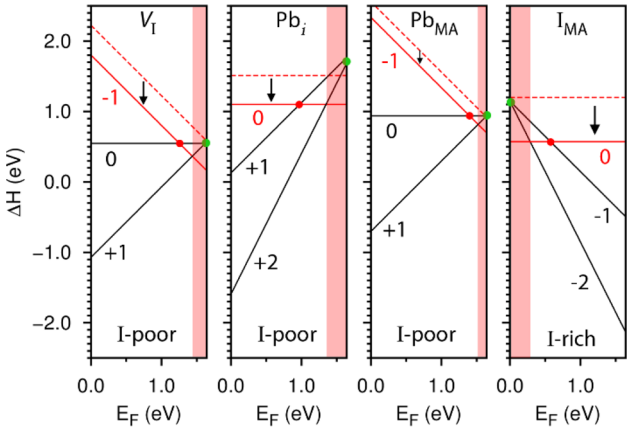

Figure 6. Calculated defect formation energy for V_I, Pb_i, Pb_{MA} and I_{MA} at different charge states as a function of Fermi energy (E_F). The red dots mark the deep transition levels, while the green dots mark the shallow transition levels. The red dashed lines and the associated dropdown arrows show the stabilization energy before and after forming a Pb dimer or an I trimer. The shading highlights the regions of E_F that should be avoided in order to avoid the recombination centers.

the results are shown at point E′ (corresponding to I-poor growth condition) and for I_{MA} at point D′ (corresponding to I-rich growth condition). For V_I to be stable in −1 charge state, it needs to be *n*-type with E_F > 1.44 eV, as marked by a shaded region in Figure 6. Otherwise, the stable charge state becomes +1, which has a very shallow $\varepsilon(0/+)$ level as marked by a green dot in Figure 6 and cannot be a RC. For Pb_i, its formation energy is higher than V_I. However, because of its relatively larger stabilization energy, as marked by the dropdown arrow from the red dashed line in Figure 6, due to the formation of a Pb dimer, Pb_i requires less *n*-type (i.e., E_F > 1.35 eV) to be stabilized in the neutral charge state. So, it could also become an important RC in the region with E_F > 1.35 eV but <1.44 eV. Pb_{MA} shows similar behavior to V_I, but both its formation energy and the required E_F are higher than that of V_I. Therefore, its role as a RC will be mostly shadowed by V_I. For I_{MA} to be a RC, it requires the material to be *p*-type with E_F < 0.29 eV. Overall, to prevent these deep levels from being effective RCs, it is required to confine E_F in the region not too close to the band edges, namely in the region from about 0.29 to 1.35 eV, which correspond to equilibrium majority carrier concentration lower than 4×10^{13} cm^{-3} at 300 K.

Lifetime of Non-equilibrium Carriers. The Fermi energy range from 0.29 to 1.35 eV obtained above provides a sufficient condition to avoid the recombination centers because in this range the deep transition levels do not form. If the Fermi level

dx.doi.org/10.1021/ja5079305 | J. Am. Chem. Soc. 2014, 136, 14570−14575

is located outside this range, the lifetime (τ) of the non-equilibrium carriers due to non-radiative recombination through the deep transition levels can be estimated on the basis of SRH theory. By definition, $\tau = \Delta n/G = \Delta p/G$, with $\Delta n = \Delta p$ the concentration of non-equilibrium carriers and G the external generation rate due to light absorption. Here, the total lifetime due to the four different deep-level defects can be obtained by $1/\tau = 1/\tau(V_I) + 1/\tau(Pb_i) + 1/\tau(Pb_{MA}) + 1/\tau(I_{MA})$. For each defect, the relation between Δn and G at steady state is given by[28]

$$G = (np - n_i p_i)/[\tau_{h,min}(n + n_D) + \tau_{e,min}(p + p_D)]$$

where n represents the total electron concentration, i.e., the sum of equilibrium concentration (n_0) and non-equilibrium concentration (Δn), n_i represents the intrinsic electron concentration, and n_D represents the electron concentrations contributed by the RCs. The notations are similar for holes. $\tau_{e,min}$ and $\tau_{h,min}$ represent the minimal lifetime of electrons and holes, respectively, between generation and capture by the RCs.

Figure 7 shows the calculated lifetime τ as a function of the chemical potentials in the allowed range from point E′ (I-poor condition) to point D′ (I-rich condition). Numerical details for generating the plots are presented in the Supporting Information. Figure 7a is obtained at the limit of large capture cross sections (i.e., 10^{-12} cm^2 for attractive centers and 10^{-15} cm^2 for neutral centers), while Figure 7b is obtained at the limit of small capture cross sections (i.e., 10^{-15} cm^2 for attractive centers and 10^{-17} cm^2 for neutral centers).[29] We consider both an n-type and a p-type condition with E_F at 0.05 eV below the CBM and above the VBM, respectively.

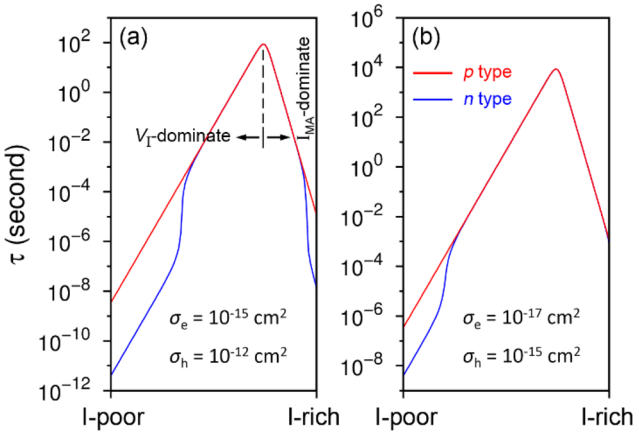

Figure 7. Lifetime ($\tau = \Delta n/G = \Delta p/G$) of non-equilibrium carriers estimated according to the SRH theory at the limit of large (a) and small (b) capture cross sections, σ_e and σ_h. Note that the deep $\varepsilon(0/-)$ levels for both V_I and I_{MA} are attractive centers to holes and neutral centers to electrons. The red and blue curves represent an n-type ($E_F = E_{CBM} - 0.05$ eV) and a p-type ($E_F = E_{VBM} + 0.05$ eV) case, respectively.

As seen in Figure 7, the lifetime is mainly limited by V_I in the I-poor condition, while in the I-rich condition the lifetime is mainly limited by I_{MA}. The Pb_i and Pb_{MA} defects do not play a significant role in the recombination because of their relative large formation energy. Under the n-type condition, transitions from the region dominated by $\tau_{h,min}$, where $\Delta p \ll n_0$, to the region dominated by $\tau_{e,min}$, where $\Delta p \gg n_0$, can be observed. At the limit of large capture cross section, the lifetime could be as low as 4×10^{-12} second under n-type condition, while at the limit of small capture crosssection, the smallest lifetime is about 4×10^{-9} s. For efficient carrier extraction with the absorber layer of about 1 μm thickness, it is required that the lifetime is at least a couple of tenths of microseconds.[12] It is therefore desirable to avoid the I-poor condition and preferably the I-rich too if the capture cross-section is large.

As a remark, it should be mentioned that the analysis above on lifetime is based purely on the defect thermodynamics. However, as the strict thermodynamic equilibrium may not be achieved in typical growth techniques, a larger concentration of the deep-level defects than that allowed by thermodynamics could exist in the material. Therefore, the actual role of the RCs in recombination should be identified through close cooperation with experimental work.

Future Work. The organic−inorganic hybrid perovskites are a new family of solar cell materials. At the cation sites, both MA[39−43] and Pb[17,18] have been substituted successfully for making solar cells with promising efficiency. At the anion sites, mixing I with Cl has been found to be critical for boosting the efficiency.[12] The effect of mixing Cl at anion sites can be understood in terms of the possible reduction of the RCs due to the V_I defects because the strain energy penalty for forming the Pb-dimer is increased due to the larger electronegativity of Cl than I. The effect of substitution at cation sites, e.g., by Sn, is not obvious. Our preliminary study on $MASnI_3$ also suggests the formation of Sn-dimers, while the corresponding transition levels is not as deep as that for $MAPbI_3$. However, the calculation on $MASnI_3$ is more prone to the band gap error of the DFT calculation. More conclusive results require higher level methods, such as GW method and hybrid functional calculations, which are still challenging for the supercell size employed in the present study.

CONCLUSIONS

In summary, first-principles calculations unveil the important defect chemistry and physics of perovskite solar cell materials. Our study reveals strong covalency of both the Pb cations and I anions in $CH_3NH_3PbI_3$, which is responsible for the formation of Pb dimers or I trimers in intrinsic defects V_I, Pb_i, Pb_{MA}, and I_{MA}. Stabilization of such defects by the strong covalency at certain charge states gives rise to deep transition levels within the band gap, which could serve as recombination centers detrimental to solar cell performance. Our study further suggests that controlling the Fermi energy position of the material could help to avoid such recombination centers. The findings from this study are qualitatively different from those of previous studies following the standard treatment of traditional semiconductors, which have suggested weak covalency and the absence of deep-level defects in $CH_3NH_3PbI_3$. The new understanding provided in this work is expected to shed light on the future design of perovskite-based solar cells with higher efficiency and using environmentally friendly elements.

ASSOCIATED CONTENT

Supporting Information

Numerical details used for obtaining Figures 5 and 7. This material is available free of charge via the Internet at http://pubs.acs.org.

AUTHOR INFORMATION

Corresponding Authors

suny4@rpi.edu (Y.-Y.S.)
zhangs9@rpi.edu (S.Z.)

Notes

The authors declare no competing financial interest.

■ ACKNOWLEDGMENTS

Y.-Y.S. and H.Z. acknowledge support by the National Science Foundation under Grant No. DMR-1104994. M.L.A. and S.Z. acknowledge support by the U.S. Department of Energy (DOE) under Grant No. DE-SC0002623. Supercomputer time was provided by the National Energy Research Scientific Computing Center (NERSC) under DOE Contract No. DE-AC02-05CH11231 and the Center for Computational Innovations (CCI) at RPI.

■ REFERENCES

(1) Burschka, J.; Pellet, N.; Moon, S. J.; Humphry-Baker, R.; Gao, P.; Nazeeruddin, M. K.; Grätzel, M. *Nature* **2013**, *499*, 316−319.
(2) Liu, M.; Johnston, M. B.; Snaith, H. J. *Nature* **2013**, *501*, 395−398.
(3) Zhou, H.; Chen, Q.; Li, G.; Luo, S.; Song, T.-B.; Duan, H.-S.; Hong, Z.; You, J.; Liu, Y.; Yang, Y. *Science* **2014**, *345*, 542−546.
(4) Jeon, N. J.; Lee, H. G.; Kim, Y. C.; Seo, J.; Noh, J. H.; Lee, J.; Seok, S. I. *J. Am. Chem. Soc.* **2014**, *136*, 7837−7840.
(5) Chen, Q.; Zhou, H.; Hong, Z.; Luo, S.; Duan, H. S.; Wang, H. H.; Liu, Y.; Li, G.; Yang, Y. *J. Am. Chem. Soc.* **2014**, *136*, 622−625.
(6) Docampo, P.; Ball, J. M.; Darwich, M.; Eperon, G. E.; Snaith, H. J. *Nature Commun.* **2013**, *4*, 2761.
(7) Liu, D.; Kelly, T. L. *Nat. Photonics* **2014**, *8*, 133−138.
(8) Kojima, A.; Teshima, K.; Shirai, Y.; Miyasaka, T. *J. Am. Chem. Soc.* **2009**, *131*, 6050−6051.
(9) Zhang, S. B.; Wei, S. H.; Zunger, A.; Katayama-Yoshida, H. *Phys. Rev. B* **1998**, *57*, 9642−9656.
(10) Li, C.; Wu, Y.; Poplawsky, J.; Pennycook, T. J.; Paudel, N.; Yin, W.; Haigh, S. J.; Oxley, M. P.; Lupini, A. R.; Al-Jassim, M.; Pennycook, S. J.; Yan, Y. *Phys. Rev. Lett.* **2014**, *112*, No. 156103.
(11) Xing, G.; Mathews, N.; Sun, S.; Lim, S. S.; Lam, Y. M.; Grätzel, M.; Mhaisalkar, S.; Sum, T. C. *Science* **2013**, *342*, 344−347.
(12) Stranks, S. D.; Eperon, G. E.; Grancini, G.; Menelaou, C.; Alcocer, M. J. P.; Leijtens, T.; Herz, L. M.; Petrozza, A.; Snaith, H. J. *Science* **2013**, *342*, 341−344.
(13) Gonzalez-Pedro, V.; Juarez-Perez, E. J.; Arsyad, W. S.; Barea, E. M.; Fabregat-Santiago, F.; Mora-Sero, I.; Bisquert, J. *Nano Lett.* **2014**, *14*, 888−893.
(14) Suarez, B.; Gonzalez-Pedro, V.; Ripolles, T. S.; Sanchez, R. S.; Otero, L.; Mora-Sero, I. *J. Phys. Chem. Lett.* **2014**, *5*, 1628−1635.
(15) De Wolf, S.; Holovsky, J.; Moon, S. J.; Löper, P.; Niesen, B.; Ledinsky, M.; Haug, F. J.; Yum, J. H.; Ballif, C. *J. Phys. Chem. Lett.* **2014**, *5*, 1035−1039.
(16) Frost, J. M.; Butler, K. T.; Brivio, F.; Hendon, C. H.; van Schilfgaarde, M.; Walsh, A. *Nano Lett.* **2014**, *14*, 2584−2590.
(17) Hao, F.; Stoumpos, C. C.; Cao, D. H.; Chang, R. P. H.; Kanatzidis, M. G. *Nat. Photonics* **2014**, *8*, 489−494.
(18) Noel, N. K.; Stranks, S. D.; Abate, A.; Wehrenfennig, C.; Guarnera, S.; Haghighirad, A. A.; Sadhanala, A.; Eperon, G. E.; Johnston, M. B.; Petrozza, A. M.; Herz, L. M.; Snaith, H. J. *Energy Environ. Sci.* **2014**, *7*, 3061−3068.
(19) Yin, W. J.; Shi, T.; Yan, Y. *Appl. Phys. Lett.* **2014**, *104*, No. 063903.
(20) Kim, J.; Lee, S. H.; Lee, J. H.; Hong, K. H. *J. Phys. Chem. Lett.* **2014**, *5*, 1312−1317.
(21) Kresse, G.; Furthmüller, J. *Comput. Mater. Sci.* **1996**, *6*, 15−50.
(22) Perdew, J. P.; Burke, K.; Ernzerhof, M. *Phys. Rev. Lett.* **1996**, *77*, 3865−3868.
(23) Qiu, J.; Qiu, Y.; Yan, K.; Zhong, M.; Mu, C.; Yan, H.; Yang, S. *Nanoscale* **2013**, *5*, 3245−3248.
(24) Umari, P.; Mosconi, E.; De Angelis, F. *Sci. Rep.* **2014**, *4*, 4467.
(25) Brivio, F.; Butler, K. T.; Walsh, A.; van Schilfgaarde, M. *Phys. Rev. B* **2014**, *89*, No. 155204.
(26) Poglitsch, A.; Weber, D. *J. Chem. Phys.* **1987**, *87*, 6373−6378.
(27) Kresse, G.; Joubert, D. *Phys. Rev. B* **1999**, *59*, 1758−1774.
(28) Würfel, P. *Physics of Solar Cells: From Principles to New Concepts*; Wiley-VCH Verlag: Weinheim, 2005; p 71.
(29) Mayer, J. W.; Lau, S. S. *Electronic Materials Science: For Integrated Circuits in Si and GaAs*; Prentice Hall: Englewood Cliffs, NJ, 1989; p 161.
(30) Zhang, S. B. *J. Phys.: Condens. Matter* **2002**, *14*, R881.
(31) Van de Walle, C. G.; Neugebauer, J. *J. Appl. Phys.* **2004**, *95*, 3851.
(32) Wei, S.-H. *Comput. Mater. Sci.* **2004**, *30*, 337.
(33) Shi, L.; Wang, L. W. *Phys. Rev. Lett.* **2012**, *109*, No. 245501.
(34) Xu, H.; Sun, Y. Y.; Li, Y. G.; Feng, Y. P.; Wee, A. T. S.; Huan, A. C. H. *Phys. Rev. B* **2004**, *70*, 081313.
(35) Zhang, S. B.; Northrup, J. E. *Phys. Rev. Lett.* **1991**, *67*, 2339−2342.
(36) Yamamuro, O.; Matsuo, T.; Suga, H.; David, W. I. F.; Ibberson, R. M.; Leadbetter, A. J. *Acta Crystallogr.* **1992**, *B48*, 329−336.
(37) Bordas, J.; Robertson, J.; Jakobsson, A. *J. Phys. C: Solid State Phys.* **1978**, *11*, 2607−2621.
(38) van Bolhuis, F.; Koster, P. B.; Migchelsen, T. *Acta Crystallogr.* **1967**, *23*, 90−91.
(39) Stoumpos, C. C.; Malliakas, C. D.; Kanatzidis, M. G. *Inorg. Chem.* **2013**, *52*, 9019−9038.
(40) Koh, T. M.; Fu, K.; Fang, Y.; Chen, S.; Sum, T. C.; Mathews, N.; Mhaisalkar, S. G.; Boix, P. P.; Baikie, T. *J. Phys. Chem. C* **2014**, *118*, 16458−16462.
(41) Pang, S.; Hu, H.; Zhang, J.; Lv, S.; Yu, Y.; Wei, F.; Qin, T.; Xu, H.; Liu, Z.; Cui, G. *Chem. Mater.* **2014**, *26*, 1485−1491.
(42) Eperon, G. E.; Stranks, S. D.; Menelaou, C.; Johnston, M. B.; Herz, L. M.; Snaith, H. J. *Energy Environ. Sci.* **2014**, *7*, 982−988.
(43) Pellet, N.; Gao, P.; Gregori, G.; Yang, T.-Y.; Nazeeruddin, M. K.; Maier, J.; Grätzel, M. *Angew. Chem., Int. Ed.* **2014**, *53*, 3151−3157.